Journal of Materials Chemistry

Cite this: J. Mater. Chem., 2012, 22, 19031

www.rsc.org/materials

PAPER

Fabrication of hollow core carbon spheres with hierarchical nanoarchitecture for ultrahigh electrical charge storage†

Baizeng Fang,[abc] Jung Ho Kim,[a] Min-Sik Kim,[a] Arman Bonakdarpour,[bc] Alfred Lam,[bc] David P. Wilkinson*[bc] and Jong-Sung Yu*[a]

Received 29th May 2012, Accepted 18th July 2012
DOI: 10.1039/c2jm33435f

A simple and reproducible sol–gel synthesis strategy was developed to fabricate hollow core carbon spheres (HCCSs) with hierarchical nanoarchitecture through the hydrolysis, self-assembly and co-condensation of bis-[3-(triethoxysilyl)propyl]disulfide (TESPDS) and octadecyltrimethoxysilane (C_{18}TMS). This synthesis route allows one to fabricate thioether-bridged organosilica (TBOS) with tailored spherical structure and particle size which can be further converted to HCCS upon calcination under N_2 flow. It is assumed that hydrophobic octadecyl chains of hydrolyzed C_{18}TMS first form a micelle-like self-assembly structure with hydrophilic trihydroxysilyl groups as heads, and a reactive core is then expanded by the base-catalyzed co-condensation of TESPDS and/or C_{18}TMS over the C_{18}TMS self-assembly structure. The organic moieties of TESPDS and C_{18}TMS not only serve as a porogen during the formation of TBOS but also as a carbon precursor for transformation of TBOS into HCCS during the carbonization. Due to its unique hierarchical nanostructure composed of hollow macroporous core and meso/microporous shell, which facilitates fast mass transport, along with large surface area for electrical charge storage, the HCCS for the first time exhibits ultrahigh specific capacitance and energy, good cycling performance and rate capability.

Introduction

Nanostructured carbon materials with hierarchical porosity, particularly mesopores in combination with macropores/micropores, are attracting much interest due to their potential applications as sorbents,[1] in separation and filtration,[2] photonic crystals,[3] catalyst supports for low temperature fuel cells,[4–6] sensors, electrode materials for electrochemical capacitors,[7–9] lithium ion batteries,[10–12] solar cells,[13,14] hydrogen storage systems,[15–17] and in other emerging nanotechnologies. Hierarchical nanostructured materials that contain interconnected macroporous/mesoporous and mesoporous/microporous structures have demonstrated enhanced properties compared with single-pore-sized porous materials due to improved mass transport through the macropores/mesopores and enhanced selectivity and maintenance of specific surface area on the level of fine pore systems through micropores/mesopores.[18–29] Therefore, from the viewpoint of practical applications, hierarchical nanostructured carbons (HNCs) with combined macro/mesoporous porosity are of particular significance and interest because particular applications can be tailored through controllable synthesis of HNCs with designed nanostructures. The most commonly used technique for creating HNCs is "nanocasting", a technique that involves first the creation of a sacrificial hierarchical nanostructured material, *i.e.*, liquid crystal,[30] polymer latices,[31] or silica[32–34] template with a hierarchical porous nanostructure, followed by the impregnation of the template with an appropriate carbon source, carbonization and subsequent removal of the template. Although a variety of HNC frameworks with tailored pore structures can be created through nanocasting using hierarchical nanostructured silicas (HNSs) as templates, some challenges still remain. For example, one challenge is the efficient fabrication of a HNS framework with tailored nanostructure and hierarchical porosity of meso/macropores.

Hollow core–mesoporous shell carbon (HCMSC) is one of the most interesting HNCs, which has demonstrated very promising applications in gas sorbents,[1] hydrogen storage,[18] fuel cells,[5,19,33] solar cells,[13,35,36] and so on. However, traditional fabrication of HCMSC spheres involves prior preparation of solid core–mesoporous shell (SCMS) silica,[33,37–39] which makes the whole synthesis process complicated and time-consuming. Recently, Fu *et al.* reported simpler synthesis of hollow core–porous shell

[a]Department of Advanced Materials Chemistry, WCU Research Team, Korea University, 2511 Sejong-ro, Sejong City 339-700, Republic of Korea. E-mail: jsyu212@korea.ac.kr
[b]Department of Chemical & Biological Engineering, University of British Columbia, 2360 East Mall, Vancouver, B.C., Canada V6T 1Z3
[c]Clean Energy Research Center, 2360 East Mall, Vancouver, B.C., Canada V6T 1Z3. E-mail: dwilkinson@chbe.ubc.ca

† Electronic supplementary information (ESI) available: Details on the synthesis of "pure" silica, TGA curve for the HCCS, nitrogen adsorption–desorption isotherms for activated carbon (Norit SX Plus) and carbon black Pearls 2000. See DOI: 10.1039/c2jm33435f

carbon spheres by the pyrolysis of core–shell polystyrene (PS)–cross-linked polyphosphazene composites.[40] The core size of the carbon spheres was controlled by the PS template size, which is generally so large (*i.e.*, usually larger than 300 nm for commercially available PS spheres) that it may result in high electrical resistance as an electrode material. Alternatively, large quantity of micropores (*i.e.*, less than 0.7 nm in diameter) could be produced through the pyrolysis of polystyrene–cross-linked polyphosphazene composites, but this would limit their application where fast mass transport is required.

In this study, a novel synthesis strategy as shown in Fig. 1 has been developed for fabrication of hollow core carbon spheres (HCCSs) with tailored hierarchical nanoarchitecture. The novel synthesis strategy of HCCSs generates *in situ* spherical thioether-bridged organosilica (TBOS) through the hydrolysis, self-assembly and co-condensation of bis-[3-(triethoxysilyl)propyl] disulfide (TESPDS) and octadecyltrimethoxysilane (C_{18}TMS). This novel synthesis strategy is much simpler and time-saving compared with the traditional synthesis method[33] and even simpler than the method recently developed by Fu *et al.*[40] More interestingly and importantly, through careful control of dosages of TESPDS and C_{18}TMS in the reaction solution, HCCSs with various hollow core size–mesoporous shell thickness can be produced readily and thus tailored to particular applications. As a typical application, HCCS was explored as an electrode material for electric double layer capacitors (EDLCs). The unique structural characteristics of the 3D interconnected nanostructure with hierarchical porosity provide large specific surface area (*i.e.*, large active sites) for electrical charge storage as well as highly developed hierarchical macro/meso porosity for fast mass transport. The HCCS has for the first time demonstrated enormous improvement in EDLC performance compared with its counterparts such as activated carbon (Norit SX Plus) and carbon black Pearls 2000.

Experimental section

Synthesis of TBOS spheres and HCCS

A schematic synthesis of TBOS spheres and HCCS is illustrated in Fig. 1. Typically, a solution containing 10 ml of TESPDS and 6 ml of C_{18}TMS was added to a co-solvent solution including 200 ml of ethanol, 600 ml of deionized (DI) water and 12 ml of aqueous ammonia (28 wt%) and stirred for several hours. The solid product was retrieved by centrifugation and dried at 80 °C overnight followed by calcination under N_2 flow at 350 °C for 2 h and carbonization at 800 °C for 6 h. Silica was etched off by 2.0 M NaOH at 60 °C from the as-prepared carbon–silica composite, and HCCS was collected after washing the residue in EtOH–H_2O solution (EtOH/H_2O = 1 : 1 in volume ratio).

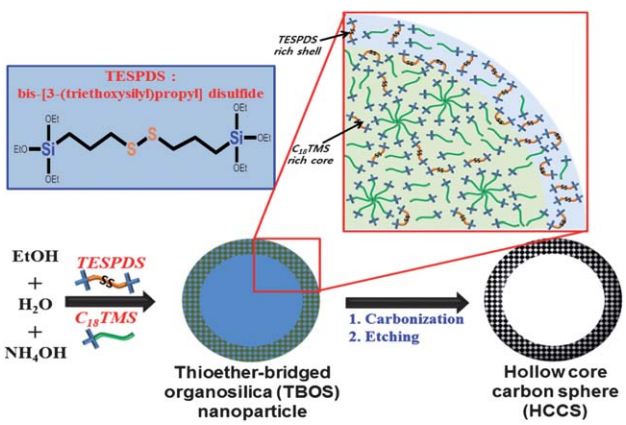

Fig. 1 Schematic illustration of the fabrication of hollow core carbon sphere (HCCS).

The fabrication of carbon electrodes was as follows: carbon (active material), graphite powder (conductivity enhancing material) and polytetrafluoroethylene (PTFE, binder) were mixed in a mass ratio of 90 : 6 : 4 and dispersed in deionized water (the mass ratio of carbon to water was set to be 1 : 3). After stirring for a couple of hours, the slurry was pasted onto a carbon paper of 16 mm diameter (as a current collector). The carbon-coated carbon paper was then dried under vacuum at 120 °C for *ca.* 12 h prior to use. The mass of carbon in the carbon electrode was *ca.* 4.0 mg.

Characterization

N_2 adsorption and desorption isotherms were measured at 77 K on a KICT SPA-3000 Gas Adsorption Analyzer after the sample was degassed at 423 K to 20 mTorr for 12 h. The specific surface areas were determined from nitrogen adsorption using the Brunauer–Emmett–Teller (BET) method. Total pore volumes (V_{total}) were determined from the amount of gas adsorbed at the relative pressure of 0.99. Micropore volume (V_{micro}) and micropore size of the porous carbons were calculated from the analysis of the adsorption isotherms using the Horvath–Kawazoe (HK) method. Pore size distribution (PSD) was calculated from the adsorption branches by the Barrett–Joyner–Halenda (BJH) method.

Surface morphologies of the porous silica and carbon were examined by a scanning electron microscope (SEM) (Hitachi S-4700) operated at an acceleration voltage of 10 kV. The microscopic features of the samples were observed with a transmission electron microscope (TEM) operated on EM 912 Omega microscope at 120 kV.

The TBOS silica spheres fabricated through the synthesis strategy illustrated in Fig. 1 and the SCMS silica produced as described in our previous papers[5,19] without TESPDS (hereafter referred to as "pure" silica for simplicity and better understanding) were characterized by Fourier transform infrared (FT-IR) spectroscopy to ascertain the grafting of organic groups on the TBOS silica, which was recorded on a NICOLET FT-IR. Each of the IR spectra was the average of 32 scans at a speed of 2 s per scan. The resolution of the spectrometer was set to 4 cm^{-1}.

All electrochemical measurements were carried out with a coin-type two-electrode cell, in which a separator soaked with 200 μL of non-aqueous electrolyte solution (1.0 M Et_4NBF_4–acetonitrile (AN)) was sandwiched between two carbon electrodes. During the electrochemical measurements, one electrode of the cell was used as a positive electrode and another one as a negative electrode. Electrochemical impedance spectroscopy measurements were carried out in the range of 100 kHz to 10 mHz with an ac amplitude of 10 mV and a dc potential of 100 mV. Specific capacitance of an electrode material is defined as electrode capacitance per unit mass active material in the

electrode. The specific capacitances derived from the constant current charge–discharge tests were calculated from the slopes of straight lines of the discharge branches according to $C = I\Delta t/\Delta V$, where I is the discharge current (in amperes) and Δt is the time period (in seconds) for the voltage change (ΔV, in volts). The specific capacitance shown against the cycle number was obtained at a constant current density of 6 mA cm^{-2}. Energy delivered to a load (E_{load}) by a capacitor was calculated according to the formula $E_{load} = (1/2)C[(V_{initial} - IR)^2 - V_{final}^2]$,[41] where $V_{initial}$, V_{final}, I, and R stands for the initial voltage limit, final voltage limit, discharge current, and direct current internal resistance of a discharge process, respectively. Specific energy of a capacitor was defined as the energy delivered to a load (*i.e.*, E_{load}) divided by total mass of the active material in two electrodes. *IR* drop was collected at the beginning of the discharge process.

Results and discussion

The TBOS silica spheres fabricated through the synthesis strategy illustrated in Fig. 1 were nonporous dense particles as confirmed by SEM and TEM images (figure not shown). Fig. 2 presents typical SEM and TEM images for the TESPDS-derived HCCSs. The SEM image shows that the HCCSs are generated as uniform individual discrete particles with a particle diameter of *ca.* 200 nm. The TEM image reveals that HCCSs possess a core of *ca.* 140 nm and a shell thickness of *ca.* 30 nm, which is in good agreement with that observed from the SEM image. TGA analysis for the HCCS shown in Fig. S1 (ESI†) reveals that almost all silica has been successfully removed from the TESPDS-derived composite of silica–carbon.

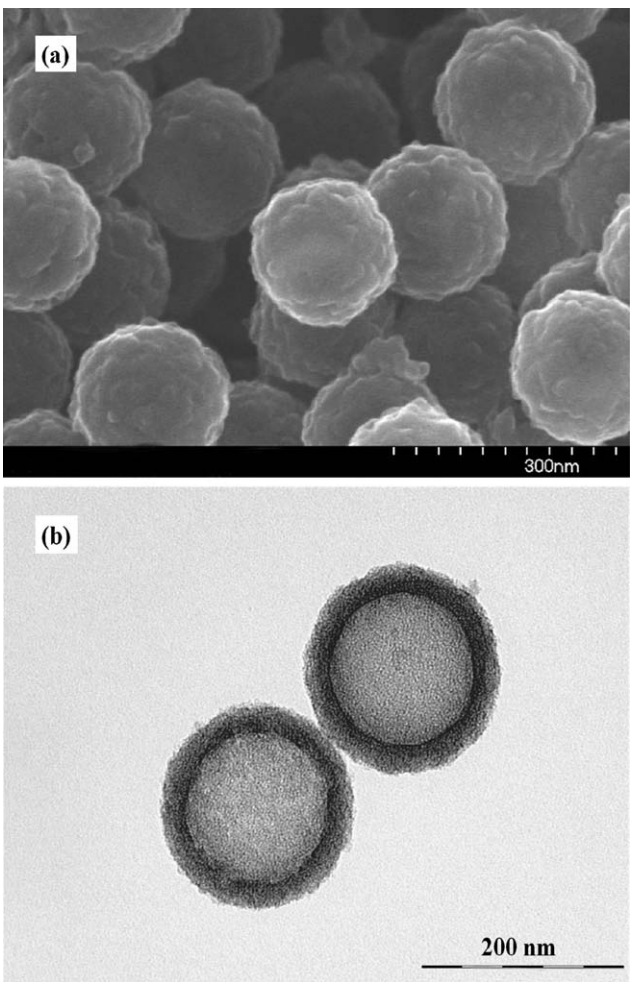

Fig. 2 SEM (a) and TEM (b) images of HCCS.

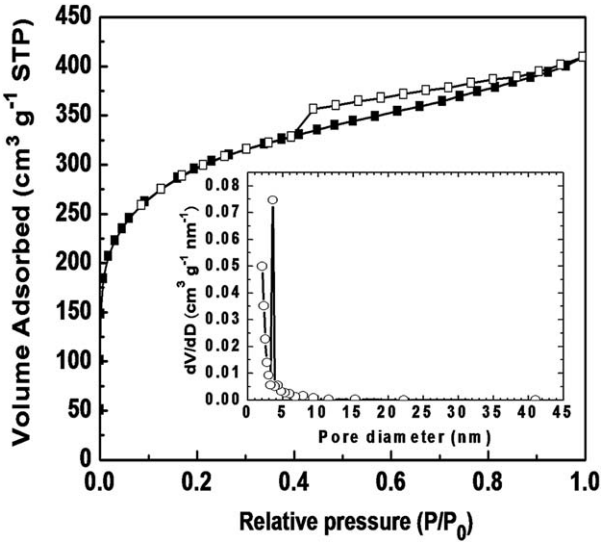

Fig. 3 Typical nitrogen adsorption–desorption isotherm at 77 K and the derived PSD for HCCS.

The nitrogen adsorption–desorption isotherm shown in Fig. 3 for the HCCSs can be classified as a type IV isotherm with a type H_2 hysteresis, according to the International Union of Pure and Applied Chemistry (IUPAC) nomenclature and suggests a narrow pore size distribution (PSD) for the HCCSs. The pore size was estimated to be *ca.* 3.5 nm from the PSD maximum. The HCCS exhibits a high surface area of 987 $m^2\ g^{-1}$ and a total pore volume of 1.01 $cm^3\ g^{-1}$, which are mainly attributable to the presence of the mesopores (2 nm < pore size < 50 nm) in the shell (mesopore volume: 0.71 $cm^3\ g^{-1}$, *ca.* 70% of the total pore volume). Table 1 summarizes surface structural parameters for the HCCS, and also for activated carbon (Norit SX Plus) and carbon black Pearls 2000, which were investigated as electrode materials for EDLC for comparison.

The formation mechanism of TBOS and HCCS can be simply explained as follows. Ethoxysilane (–Si–OC_2H_5) or methoxysilane (–Si–OCH_3) groups of TESPDS or C_{18}TMS hydrolyze to form silanol group (–Si–OH), which can be accelerated by hydroxide ions in the system. The resulting silanol group further

Table 1 Surface structural parameters derived from N_2 adsorption–desorption isotherms for various carbon materials, *i.e.*, HCCS, activated carbon Norit SX Plus and carbon black Pearls 2000

Sample	S_{BET} ($m^2\ g^{-1}$)	V_{micro} ($cm^3\ g^{-1}$)	V_{meso} ($cm^3\ g^{-1}$)	V_{total} ($cm^3\ g^{-1}$)	PSD (nm)
HCCS	987	0.30	0.71	1.01	3.5
SX Plus	1082	0.43	0.55	0.98	4.6
Pearls 2000	1427	1.15	1.36	2.51	3.5

reacts with alkoxysilane or another silanol to form a siloxane linkage (–Si–O–Si–) with the release of alcohol or water. For a system containing C_{18}TMS, the silicon atoms in C_{18}TMS are more susceptible to nucleophilic attack from water or hydroxide because the disulfide bond in TESPDS is richer in electron than the octadecyl bond in C_{18}TMS, resulting in higher hydrolysis rate for C_{18}TMS. Therefore, when TESPDS is employed along with C_{18}TMS in a basic medium, the hydrophobic octadecyl chains of hydrolyzed C_{18}TMS first form a micelle-like self-assembly structure with hydrophilic trihydroxysilyl groups as heads, and the reactive core is then expanded by the base-catalyzed co-condensation of TESPDS and/or C_{18}TMS over the C_{18}TMS self-assembly structure. Because C_{18}TMS is much more reactive than TESPDS, the core is mainly composed of the base-catalyzed co-condensation of hydrolyzed C_{18}TMS molecules and partially of co-condensation between hydrolyzed C_{18}TMS and TESPDS. Through the repeated condensation, the size of particles increases, generating extended C_{18}TMS-derived silica-rich siloxane linkage (–Si–O–Si–) in the core area. When C_{18}TMS concentration becomes lower, TESPDS is gradually more involved in condensation, and can assemble on the outer surface of the C_{18}TMS-rich core. In this case, organic octadecyl bonds and $–(CH_2)_3–S_2–(CH_2)_3–$ moieties interact/self-assemble heavily on the outer surface of the core. This self-assembly structure generates TBOS with interesting inorganic–organic hybrid core–shell like structure. In particular, excess TESPDS polymerizes/condenses with C_{18}TMS over the silica-rich core structure to form shell composition, where $–(CH_2)_3–S_2–(CH_2)_3–$ of TESPDS interact/co-assemble with C_{18}TMS (during carbonization) over the silica-rich core structure. Thus, calcination in N_2 and subsequent silica etching generate hollow carbon capsules with mesoporous shell since organic octadecyl bonds alone contribute very little to the formation of extended carbon structure if any, leaving almost nothing in the core.

FT-IR spectra shown in Fig. 4 confirm the thioether groups grafted on the TESPDS-derived silica, which reveals C–S and C–Si stretching bands at *ca.* 693 and 1250 cm^{-1}, respectively. These two stretching bands were not observed for the "pure" silica, which was fabricated using tetraethylorthosilicate (TEOS) based on a modified Stöber method[42] (details on the synthesis can be seen in the ESI†), suggesting the incorporation of TESPDS into the TBOS framework. The S–S stretching modes were also detected in wave numbers of 500–540 cm^{-1} in the TBOS. In contrast, as for the "pure" silica, only Si–O bonds, *i.e.*, the band at *ca.* 1020 cm^{-1} from Si–O–Si vibration, were observed as expected.

For the synthesis of HCCSs, the organic moiety $(–(CH_2)_3–S_2–(CH_2)_3–)$ of TESPDS works as a porogen and can be carbonized in N_2 flow to form a carbon framework. In addition, carbon can also be generated from the organic moiety (*i.e.*, $–(CH_2)_{17}–CH_3$) of C_{18}TMS, which acts as a porogen agent as well as a silica source in the synthesis of mesoporous TBOS silica.[43] After the carbonization of TBOS in N_2 followed by etching silica from the carbon–silica composite, HCCSs can be generated. The conversion of the organic moiety to carbon may be facilitated by means of sulfide group in the framework, which could considerably increase the carbon yield *via* dehydration and sulfonation reactions.[43]

According to the proposed mechanism it is clear that the core size and/or shell thickness of the HCCSs can be controlled independently through the control of dosages of TESPDS and C_{18}TMS in the reaction solution. From Fig. 5 it is evident that HCCSs can be produced with various core sizes (*i.e.*, from 105 to 190 nm) but with the same shell thickness (*i.e.*, 25 nm) or the same core size (*i.e.*, 190 nm) but with different shell thickness (*i.e.*, from 25 to 35 nm). Particularly interesting, HCCSs with very small particle size but well-defined core–shell nanostructure can also be readily produced by the synthesis strategy developed in this study (*i.e.*, 25 nm in core size and 15 nm in thickness). It was found that this HCCS has a surface area larger than 2000 $m^2 g^{-1}$ while mesopores size remains similar to that of other HCCSs (*ca.* 3.5 nm). High specific surface area, large mesoporous volume and particularly the unique core–shell nanostructure make HCCS an ideal candidate for electrode materials in energy-related applications.

EDLC is a unique electrical storage device which can store much more energy than conventional capacitors and offer much higher power density than batteries, and is thus considered to

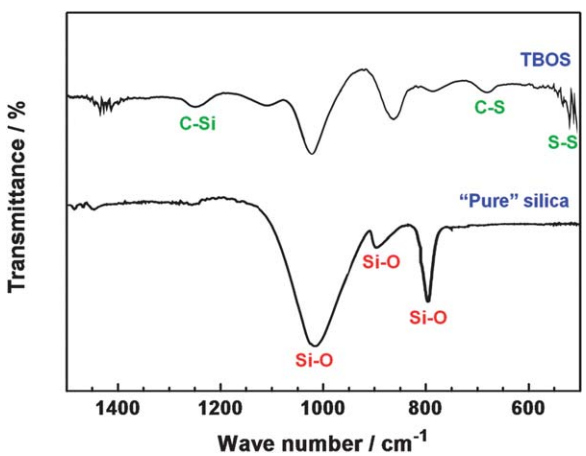

Fig. 4 FT-IR spectra for "pure" silica and thioether-bridged organo-silica (TBOS).

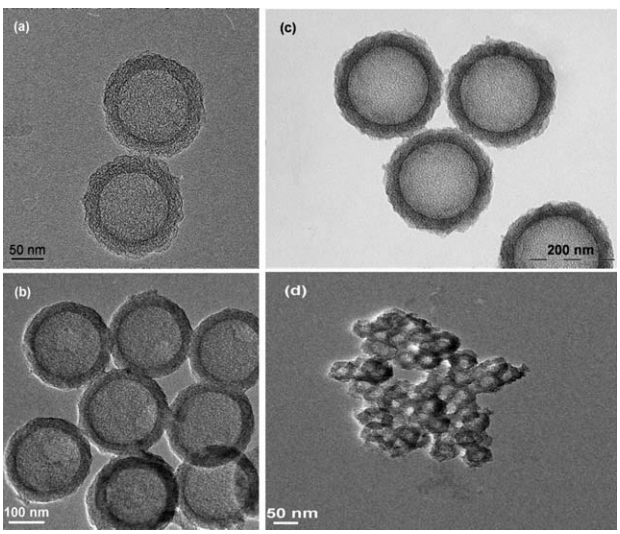

Fig. 5 TEM/HRTEM images for HCCSs with various core size/shell thickness (nm) including (a) 105/25, (b) 190/25, (c) 190/35 and (d) 25/15.

occupy a position somewhere between batteries and capacitors. In the past decades, porous carbonaceous materials, particularly activated carbons[41,44] have been almost exclusively investigated as electrode materials for EDLCs because of their relatively low cost and high specific surface area. However, specific capacitances and energy densities obtained from such activated carbon materials are usually much lower than expected, which greatly hinders practical application of EDLCs in some areas where a high energy density is required, *i.e.*, in electric/hybrid vehicles. In recent years, novel nanostructured carbon-based electrode materials have been examined for electrochemical capacitors, *e.g.*, carbon aerogels,[45] carbon nanotubes,[46] mesoporous carbon nanofibers,[47] multiwalled carbon nanotube/manganese oxide nanocomposites,[48] vertically oriented graphene nanosheet electrodes,[49] and chemically modified graphene (CMG).[50] Compared with activated carbon materials, these nanostructured porous carbonaceous materials have demonstrated enhanced capacitive performance. Further development of nanostructured materials with high EDLC performance is still highly desired.

Fig. 6 shows representative cyclic voltammograms (CV) recorded at various scan rates for the capacitors using various carbon materials, in which the current responses (I) at various potentials have been converted to specific capacitance using the equation $C = I/(v \times m)$, where v and m stands for the scan rate and the mass of the active material, respectively. It is well known that the capacitance of an ideal supercapacitor is independent of frequency, and the electrical charge stored by a capacitor is proportional to the voltage imposed. Therefore, for a constant sweep rate (mV s^{-1}), the current response will stay constant in the case of the CV measurements. At identical scan rates particularly at high rates, more ideal capacitive behaviour was observed for the HCCS with a steeper current change at the switching potentials (*i.e.*, −1.5 and 1.5 V), resulting in a more rectangular-shaped I–V curve. An important characteristic of electrical energy storage in a capacitor is that energy is retrievable on discharging over the same potential range as that required to store the energy on charging, otherwise the energy storage is limited. The slower changes at the switching potentials in the CVs of the activated carbon (Norit SX Plus) and carbon black Pearls 2000 electrodes stem from the slower re-organization of the double layer owing to slower ionic motions in micropores. Furthermore, considerably larger capacitance was achieved for the HCCS compared with its counterparts.

Nyquist plots shown in Fig. 7a reveal depressed semicircles in the high frequency region for all the tested carbon materials, which represent a parallel combination of resistive and capacitive components. Charge-transfer resistance was estimated to be *ca.* 2.1 Ohms from the diameter of the semicircle for the HCCS, which is much smaller than that of activated carbon (*i.e.*, 4.9 Ohms) and carbon black (9.2 Ohms). The smaller resistance for the HCCS is probably related to its unique core–shell nanostructure, favouring rapid electron and mass transport. Fig. 7b presents the variation of the real part of the capacitance (C') with frequency for various carbon materials. The HCCS demonstrates the highest capacitance and the best frequency response, which is highly consistent with that observed from the CV measurements. At low frequency (*i.e.*, 10 mHz), the capacitances reach 75, 53 and 56 mF cm^{-2} for the HCCS, activated carbon and carbon black, respectively. Even at such low

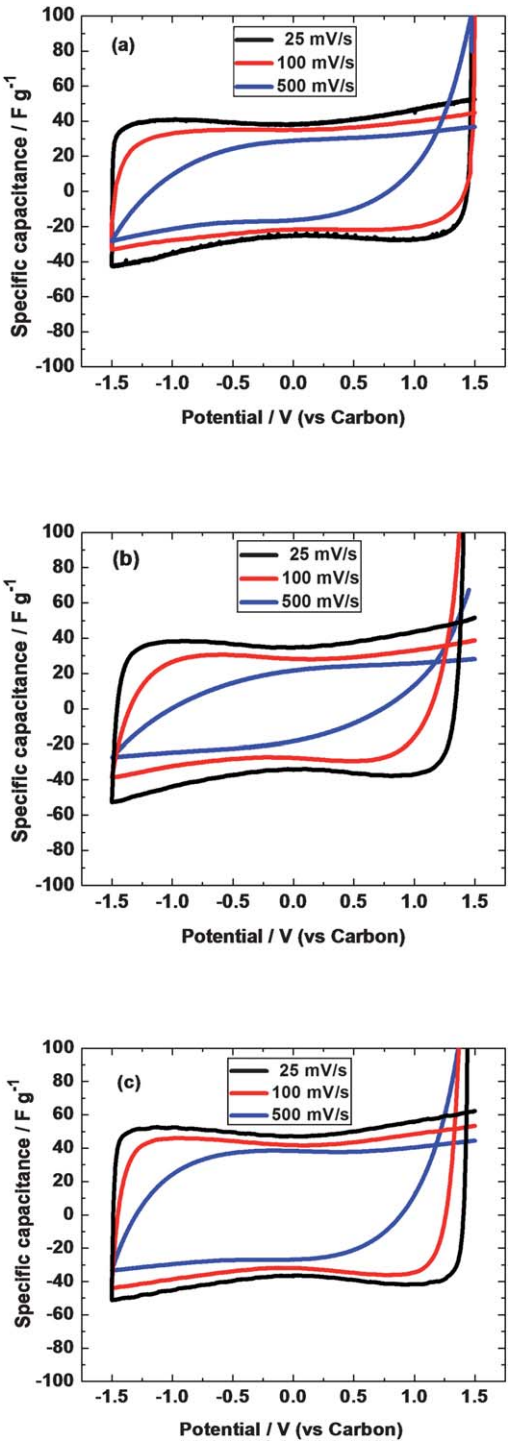

Fig. 6 Cyclic voltammograms at various scan rates for the capacitors using activated carbon (a), carbon black (b) and HCCS (c) as electrodes, where the current has been transferred into specific capacitance based on the mass (4.0 mg) of carbon.

frequency the capacitance of the carbon black does not show a clear sign of saturation, which is probably due to its larger particle size and longer diffusion paths for electrolyte ions that prevent the system from reaching the equilibrium ion adsorption within the time period. Activated carbon (Norit SX Plus) showed a bit better, but still similar behavior to that of the carbon black,

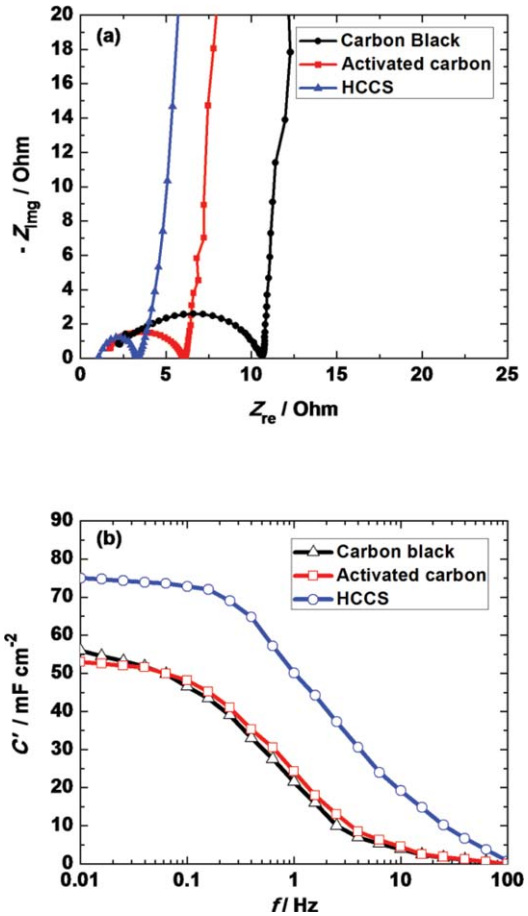

Fig. 7 Typical Nyquist plots (a) for capacitors based on various carbon materials in the frequency range of 100 kHz to 10 mHz and variation of the real part of the capacitance with the frequency (b).

which is in good agreement with that reported for activated carbon sample (YP17D, Kuraray Chemical, Osaka, Japan) by Korenblit *et al.*[51] However, it is observed that most of the electrolyte ions have reached the adsorption sites for the HCCS unlike its counterparts. In all the cases, the capacitance decreases with the increasing frequency, and at a high frequency, the EDLC acts like a pure resistor. If the highest operating frequency (*i.e.*, usable frequency) is defined as the frequency at which the capacitance is 50% of that at the lowest frequency (*i.e.*, 10 mHz), it is evident that the HCCS reveals not only better frequency response than its counterparts, but also a highest operating frequency exceeding 2 Hz, which has rarely been observed in organic electrolytes. It is well known that the change of *C*' with the frequency depends on many parameters, such as the nature of the electrolyte, the electrode thickness and the porous structure. In this study, the effects from the electrolyte and electrode thickness should be similar and thus the change of *C*' with the frequency mainly depends on the porous structure of electrode materials. Much higher capacitance (about twice) at low-mid frequency and better frequency response have been demonstrated by the HCCS, implying that the unique core–shell nanostructure with hierarchical porosity favours fast mass and electrical charge transfer.

Representative constant current charge–discharge behaviours are shown in Fig. 8 for various carbon materials. At a relatively

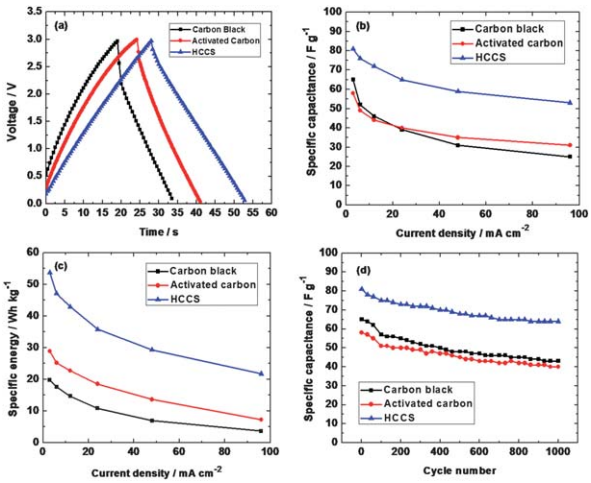

Fig. 8 Voltage shown against time for constant current charge–discharge at 6 mA cm^{-2} (a), specific discharge capacitances (b) and specific energies (c) at various current densities, and the variation of specific capacitance with cycle number at 6 mA cm^{-2} (d).

low charge–discharge rate, *i.e.*, 6 mA cm^{-2}, a considerably smaller *IR* drop, which can be observed from the initial discharge, was found for the HCCS compared with the other porous carbon materials. A decrease in the *IR* drop, namely, a decrease in the polarization resistance *R*, is primarily attributable to the improved electron and mass transport. The decrease in the *IR* drop contributes a lot to the usable voltage window for discharge, and thus higher discharge capacity (energy) can be expected. This is very evident from the variation of specific capacitance and energy with discharging current density shown in Fig. 8b and c, respectively. With increasing discharge rate the specific capacitances decrease for all the carbon materials, which is due to the decreased sites for EDL formation. Higher capacitance and slower decay in the capacitance with increasing discharge rate were observed for the HCCS carbon, and a similar tendency was observed for the specific energy, suggesting faster mass transport within the micro/mesopores of HCCS. The impact on EDLC performance of the pore structure of the electrode materials becomes very conspicuous at a high discharge rate, *i.e.*, 96 mA cm^{-2}. The specific capacitance demonstrated by the HCCS is *ca.* twice those of the activated carbon and the carbon black, while the specific energy delivered by the HCCS is about 4–6 times higher than its counterparts. For EDLCs with an organic electrolyte, specific energy makes more sense than specific capacitance. Much higher specific energy delivered by the HCCS suggests ultrahigh electrical charge storage in this material.

The impact on specific energy is more noticeable compared with specific capacitance because energy is not only dependent on capacitance but also on usable operating voltage (*i.e.*, voltage window), which strongly depends on *IR* drop. Compared with the activated carbon and the carbon black, the much higher specific capacitance observed for the HCCS at higher discharge rates also indicates that more active sites are accessible in the HCCS to the electrolyte ions. This must be mainly attributable to the unique core–shell hierarchical nanostructure of the HCCS because the HCCS has the smallest apparent surface area as shown in Table 1. Fig. 8d reveals that HCCS also possesses better capacity retention with cycling compared with its counterparts.

It is well known that EDLC performance of electrode materials is highly dependent on the substrate (*i.e.*, current collector) used for the electrode preparation. Compared with commonly used Al foil current collector in EDLCs, carbon paper (Toray) used in this study reveals much higher electrical resistivity, which results in much larger *IR* drop (*i.e.*, voltage loss) during the charging–discharging of an EDLC, and accordingly worse EDLC properties. However, it is evident that HCCS has demonstrated much better EDLC properties compared with its counterparts, activated carbon (Norit SX Plus) and carbon black (Pearls 2000).

In this study, activated carbon Norit SX Plus reveals a specific capacitance of *ca.* 58 F g^{-1} at 6 mA cm^{-2} which is basically consistent with that reported for activated carbon materials in an organic electrolyte system. Lv *et al.* reported a specific capacitance of 55 F g^{-1} for steam-activated phenolic-based porous carbon (activation temperature: 850 °C) with a specific surface area of 1200 m^2 g^{-1}.[52] It is also interestingly noted that in an aqueous electrolyte of 5.5 M KOH, this material reveals a specific capacitance of 119 F g^{-1}, which is about twice the value observed for the organic system. It is well known that higher specific capacitances are generally obtained using aqueous electrolytes than non-aqueous electrolytes. However, a main advantage of EDLCs with non-aqueous organic electrolytes is that it is possible to obtain a higher energy density (*i.e.* specific energy) for a wider range of voltage stability.

Interestingly, in an organic system (*i.e.*, 1 M Et_4NBF_4–AN electrolyte) HCCS reveals a specific capacitance of 80 F g^{-1}, which is significantly larger than that (*i.e.*, 58 F g^{-1}) observed for activated carbon (Norit SX Plus). Even compared with that observed for other nanostructured carbon materials, the specific capacitance value (80 F g^{-1}) obtained at 6 mA cm^{-2} (*i.e.*, 3 A g^{-1} based on the mass (*i.e.*, 4 mg) of active material in each electrode) is not low. Stoller *et al.* recently investigated CMG with a BET surface area of 705 m^2 g^{-1} as EDLC electrode material.[50] With 1 M Et_4NBF_4–AN used as electrolyte, the specific capacitance obtained at 2.66 A g^{-1} was 95 F g^{-1}. Compared with the value 80 F g^{-1} at 3 A g^{-1} obtained for HCCS, slightly higher capacitance mainly results from higher electrical conductivity of the CMG material (*ca.* 200 S m^{-1}) which closely approaches that of pristine graphite and using Al foil as the current collector, both of which contribute to the much lower ESR of the capacitor.

To confirm the impact from the current collector, EDLCs with carbon electrodes using Al foil (MTI Corporation) as the current collectors were examined. To our expectation, carbon electrode materials prepared by using the MTI Al foil as the current collector reveal great improvements in EDLC performance. HCCS exhibits a specific capacitance of *ca.* 121 F g^{-1}, which is comparable to that reported by C. Vix-Guterl *et al.* for ordered porous carbon material (*i.e.*, 115 F g^{-1} for CMK-1 with a surface area of 2000 m^2 g^{-1} derived from MCM-48 template) and significantly higher than that (*i.e.*, 93 F g^{-1}) reported for CMK-3 with a surface area of 1470 m^2 g^{-1} derived from SBA-15 template,[53] and CMG (*i.e.*, 95 F g^{-1}),[50] and much higher than other controls such as activated carbon Norit SX Plus (*i.e.*, 72 F g^{-1}) and carbon black Pearls 2000 (*i.e.*, 81 F g^{-1}). Compared with ordered mesoporous carbon materials CMK-1 and CMK-3, HCCS has a much smaller specific surface area (*i.e.*, 987 m^2 g^{-1}), but demonstrates higher specific capacitance, which is mainly attributable to its unique core–shell nanostructure with hierarchical porosities, as explained below.

Larger electrical charge storage capacity, better capacity retention and higher rate capability are mainly due to the superb structural characteristics of the HCCS particularly the well-developed three-dimensionally (3D) interconnected hierarchical nanostructure composed of a hollow macro-scale core, mesoporous shell and micropores residing in the shell. In addition, the 3D interconnected large interstitial space between the packed spherical carbon particles, unique in the HCCS system, is open to the mesoporous channels. The HCCS also possesses a large surface area for efficient electrical charge storage. In particular, the hollow macroporous core can be utilized as an electrolyte solution buffering reservoir to minimize the diffusion distance to the interior surface of the mesoporous shell, while the mesoporous channels open to outer surface and to inner macroporous core in the shell form fast mass transport networks around the micropores in the shell, providing sites for the adsorption of electrical charge (storage). In addition, the large interstitial volume between the packed HCCSs is 3D interconnected and open to the mesoporous channels, providing main fast pathways for the transport of mass and electrical charge. With this hierarchical nanostructure design, three electrode processes (*i.e.*, buffering electrolyte species in the macroporous core and interstitial space, transporting electrolyte species through the mesoporous shell and interstitial space, and adsorptive electrical charge in the micropores/mesopores) involved in the EDLC can take place quickly and efficiently even at high charging–discharging rates. In addition, the buffering effect from the hollow macroporous core reduces the volume change during the charge–discharge cycling, ensuring good cycling performance. This phenomenon has also been observed for ordered multimodal porous carbon,[54] which has demonstrated good cycling performance for Li ion storage.

Conclusions

In summary, in this study a direct and simple sol–gel synthesis pathway has been developed to prepare HCCSs. Through initial hydrolysis and self-assembly of C_{18}TMS and through subsequent further co-condensation with C_{18}TMS and TESPDS, a macro-scaled core can be produced with formation of extended C_{18}TMS-derived siloxane linkage (–Si–O–Si–) framework, while relatively carbon-rich organosilica shell can be formed through self-assembly of organic octadecyl bonds and $–(CH_2)_3–S_2–(CH_2)_3–$ moieties on the C_{18}TMS-derived silica-rich core. Our present work on the synthesis of the HCCS greatly simplifies the fabrication process and can be expected to provide further insight into the facile synthesis of hierarchical nanostructured materials with a macroporous core–mesoporous shell. The as-prepared TBOS can be calcined in N_2 flow at an elevated temperature to produce the HCCS. Compared with conventional synthesis methods for HCMSCs,[28] the novel synthesis strategy here is much simpler and time-saving. More importantly, through careful control of dosages of TESPDS and C_{18}TMS in the reaction solution, HCCSs with various hollow core sizes and mesoporous shell thicknesses can be tailored and thus further enhanced EDLC performance can be expected. As an electrode material in EDLC, HCCS with a core of 140 nm and shell

thickness of *ca.* 30 nm outperforms considerably its counterparts, activated carbon (Norit SX Plus) and carbon black Pearls 2000, which is mainly attributable to its unique structural characteristics, particularly the 3D interconnected nanostructure with hierarchical porosity, not only providing large specific surface area for efficient electrical charge storage but also highly developed hierarchical macro/meso porosity for fast mass transport. The hollow macroporous core can not only work as an electrolyte solution buffering reservoir to minimize the diffusion distance, but also reduce the volume change during the charge–discharge cycling, ensuring good cycling performance.

Acknowledgements

This work was supported by NRF grant (NRF 2010-0029245) and Global Frontier R&D Program on Center for Multiscale Energy System (NRF 2011-0031571) funded by the Korea government. The authors would also like to thank the Korean Basic Science Institute at Jeonju and Chuncheon for SEM and TEM analyses. David Wilkinson would like to thank the NSERC (National Science and Engineering Research Council of Canada), the Carbon Management Canada (CMC project B222) and the Pacific Institute for Climate Solutions (PICS) for financial support, and thank David Bruce for providing chemicals.

References

1 Q.-M. Ji, S.-B. Yoon, J. P. Hill, A. Vinu, J.-S. Yu and K. Ariga, *J. Am. Chem. Soc.*, 2009, **131**, 4220–4221.
2 S. J. Sarrade, G. M. Rios and M. Carles, *Sep. Purif. Technol.*, 1998, **14**, 19–25.
3 A. Blanco, E. Chomski, S. Grabtchak, M. Ibisate, S. John, S. W. Leonardo, C. Lopez, F. Meseguer, H. Miguez, J. P. Mondia, G. A. Ozin, O. Toader and H. M. Van Driel, *Nature*, 2000, **405**, 437–440.
4 B.-Z. Fang, J.-H. Kim, M.-S. Kim and J.-S. Yu, *Chem. Mater.*, 2009, **21**, 789–796.
5 B.-Z. Fang, J.-H. Kim, M.-S. Kim, M.-W. Kim and J.-S. Yu, *Phys. Chem. Chem. Phys.*, 2009, **11**, 1380–1387.
6 B.-Z. Fang, J.-H. Kim and J.-S. Yu, *Electrochem. Commun.*, 2008, **10**, 659–662.
7 B.-Z. Fang, Y. Wei, K. Suzuki and M. Kumagai, *Electrochim. Acta*, 2005, **50**, 3616–3621.
8 B.-Z. Fang and L. Binder, *J. Power Sources*, 2006, **163**, 616–622.
9 H.-F. Yang, Q.-H. Shi, X.-Y. Liu, S.-H. Xie, D.-C. Jiang, F.-Q. Zhang, C.-Z. Yu, B. Tu and D.-Y. Zhao, *Chem. Commun.*, 2002, 2842–2843.
10 H.-S. Zhou, S.-M. Zhu, M. Hibino, I. Honma and M. Ichihara, *Adv. Mater.*, 2003, **15**, 2107–2111.
11 N. S. Ergang, J. C. Lytle, K. T. Lee, S. M. Oh, W. H. Smyrl and A. Stein, *Adv. Mater.*, 2006, **18**, 1750–1753.
12 S. Yang, X. Feng, L. Zhi, Q. Cao, J. Maier and K. Mullen, *Adv. Mater.*, 2010, **22**, 838–842.
13 B.-Z. Fang, S.-Q. Fan, J.-H. Kim, M.-S. Kim, M.-W. Kim, N. K. Chaudhari, J.-J. Ko and J.-S. Yu, *Langmuir*, 2010, **26**, 11238–11243.
14 B.-Z. Fang, M.-W. Kim, S.-Q. Fan, J.-H. Kim, D. P. Wilkinson, J.-J. Ko and J.-S. Yu, *J. Mater. Chem.*, 2011, **21**, 8742–8748.
15 G.-P. Dai, C. Liu, M. Liu, M.-Z. Wang and H.-M. Cheng, *Nano Lett.*, 2002, **5**, 503–506.
16 B.-Z. Fang, H.-S. Zhou and I. Honma, *J. Phys. Chem. B*, 2006, **110**, 4875–4880.
17 Z. Wen and J. Li, *J. Mater. Chem.*, 2009, **19**, 8707–8713.
18 B.-Z. Fang, J.-H. Kim, M.-S. Kim and J.-S. Yu, *Langmuir*, 2008, **24**, 12068–12072.
19 B.-Z. Fang, J.-H. Kim, C.-G. Lee and J.-S. Yu, *J. Phys. Chem. C*, 2008, **112**, 639–645.
20 J.-H. Kim, B.-Z. Fang, M.-Y. Song and J.-S. Yu, *Chem. Mater.*, 2012, **24**, 2256–2264.
21 G.-S. Chai, I.-S. Shin and J.-S. Yu, *Adv. Mater.*, 2004, **16**, 2057–2061.
22 K.-T. Lee, J. C. Lytle, N. S. Ergang, S. M. Oh and A. Stein, *Adv. Funct. Mater.*, 2005, **15**, 547–556.
23 G. Yushin, R.-J. Dash, J. Jagiello, J. E. Fischer and Y. Gogotsi, *Adv. Funct. Mater.*, 2006, **16**, 2288–2293.
24 Y.-S. Hu, P. Adelhelm, B. M. Smarsly, S. Hore, M. Antonietti and J. Maier, *Adv. Funct. Mater.*, 2007, **17**, 1873–1878.
25 L.-Z. Fan, Y.-S. Hu, J. Maier, P. Adelhelm, B. Smarsly and M. Antonietti, *Adv. Funct. Mater.*, 2007, **17**, 3083–3087.
26 C.-X. Guo and C.-M. Li, *Energy Environ. Sci.*, 2011, **4**, 4504–4507.
27 A. Manthiram, A. V. Murugan, A. Sarkar and T. Muraliganth, *Energy Environ. Sci.*, 2008, **1**, 621–638.
28 Z.-X. Li, J. C. Barnes, A. Bosoy, J. F. Stoddart and J. I. Zink, *Chem. Soc. Rev.*, 2012, **41**, 2590–2605.
29 P.-P. Yang, S.-L. Gai and J. Lin, *Chem. Soc. Rev.*, 2012, **41**, 3679–3698.
30 C. T. Kresge, M. E. Leonowicz, W. J. Roth, J. C. Vartuli and J. S. Beck, *Nature*, 1992, **359**, 710–712.
31 M. Antonietti, B. Berton, C. Göltner and H. Hentze, *Adv. Mater.*, 1998, **10**, 154–159.
32 J.-S. Lee, S.-H. Joo and R. Ryoo, *J. Am. Chem. Soc.*, 2002, **124**, 1156–1157.
33 S.-B. Yoon, K.-N. Sohn, J.-Y. Kim, C.-H. Shin, J.-S. Yu and T. Hyeon, *Adv. Mater.*, 2002, **14**, 19–21.
34 K. Ariga, A. Vinu, Y. Yamauchi, Q.-M. Ji and J. P. Hill, *Bull. Chem. Soc. Jpn.*, 2012, **85**, 1–32.
35 G. S. Paul, J. H. Kim, M.-S. Kim, K. Do, J. Ko and J.-S. Yu, *ACS Appl. Mater. Interfaces*, 2012, **4**, 375–381.
36 S.-Q. Fan, B.-Z. Fang, J.-H. Kim, J.-J. Kim, J.-S. Yu and J.-J. Ko, *Appl. Phys. Lett.*, 2010, **96**, 063501.
37 B.-Z. Fang, M.-S. Kim and J.-S. Yu, *Appl. Catal., B*, 2008, **84**, 100–105.
38 J.-H. Kim, B.-Z. Fang, S.-B. Yoon and J.-S. Yu, *Appl. Catal., B*, 2009, **88**, 368–375.
39 J. H. Kim and J.-S. Yu, *Phys. Chem. Chem. Phys.*, 2010, **12**, 15301–15308.
40 J.-W. Fu, Q. Xu, J.-F. Chen, Z.-M. Chen, X.-B. Huang and X.-Z. Tang, *Chem. Commun.*, 2010, **46**, 6563–6565.
41 B.-Z. Fang and L. Binder, *J. Phys. Chem. B*, 2006, **110**, 7877–7882.
42 M.-S. Kim, B.-Z. Fang, J.-H. Kim, D.-S. Yang, Y. K. Kim, T.-S. Bae and J.-S. Yu, *J. Mater. Chem.*, 2011, **21**, 19362–19367.
43 P. Valle-Vigón, M. Sevilla and A. B. Fuertes, *Chem. Mater.*, 2010, **22**, 2526–2533.
44 E. Frackowiak and F. Beguin, *Carbon*, 2001, **39**, 937.
45 B.-Z. Fang and L. Binder, *Electrochim. Acta*, 2007, **52**, 6916–6921.
46 C. Masarapu, H.-F. Zeng, K.-H. Hung and B.-Q. Wei, *ACS Nano*, 2009, **3**, 2199–2206.
47 K.-X. Wang, Y.-G. Wang, Y.-R. Wang, E. Hosono and H.-S. Zhou, *J. Phys. Chem. C*, 2009, **113**, 1093–1097.
48 S.-W. Lee, J.-Y. Kim, S. Chen, P. T. Hammond and S.-H. Yang, *ACS Nano*, 2010, **4**, 3889–3896.
49 J. R. Miller, R. A. Outlaw and B. C. Holloway, *Science*, 2010, **329**, 1637–1639.
50 M. D. Stoller, S.-J. Park, Y.-W. Zhu, J.-H. An and R. S. Ruoff, *Nano Lett.*, 2008, **8**, 3498–3502.
51 Y. Korenblit, M. Rose, E. Kockrick, L. Borchardt, L. Kvit, S. Kaskel and G. Yushin, *ACS Nano*, 2010, **4**, 1337–1344.
52 W. Lv, D.-M. Tang, Y.-B. He, C.-H. You, Z.-Q. Shi, X.-C. Chen, C.-M. Chen, P.-X. Hou, C. Liu and Q.-H. Yang, *ACS Nano*, 2009, **3**, 3730–3736.
53 C. Vix-Guterl, E. Frackowiak, K. Jurewicz, M. Friebe, J. Parmentier and F. Beguin, *Carbon*, 2005, **43**, 1293–1302.
54 B.-Z. Fang, M.-S. Kim, J.-H. Kim, S.-M. Lim and J.-S. Yu, *J. Mater. Chem.*, 2010, **20**, 10253–10259.

